Journal of Materials Processing Technology 227 (2016) 268–280

Contents lists available at ScienceDirect

Journal of Materials Processing Technology

journal homepage: www.elsevier.com/locate/jmatprotec

Influence of ring growth rate on damage development in hot ring rolling

C. Wang[a,*], H.J.M. Geijselaers[b], E. Omerspahic[c], V. Recina[c], A.H. van den Boogaard[b]

[a] Materials innovation institute (M2i), P.O. Box 5008, 2600 GA Delft, The Netherlands
[b] University of Twente, Faculty of Engineering Technology, P.O. Box 217, 7500 AE Enschede, The Netherlands
[c] SKF Group, Manufacturing Development Center, SE-415 50 Gothenburg, Sweden

ARTICLE INFO

Article history:
Received 26 March 2015
Received in revised form 16 July 2015
Accepted 15 August 2015
Available online 20 August 2015

Keywords:
Hot ring rolling
Porosity
Finite element analysis
Damage indication

ABSTRACT

As an incremental forming process of bulk metal, ring rolling provides a cost effective process route to manufacture seamless rings. In the production of hot rolled rings, defects such as porosity can sometimes be found in high alloyed steel, manufactured from ingots having macro-segregation. For the reduction of the waste of material and improvement of product quality, a better understanding of the relations between parameters in the hot ring rolling process and the occurrence of porosity is needed.

In this study round bars were used to manufacture rings on an industrial ring rolling mill. Different ring growth rates were applied to investigate the influence on the occurrence of porosity in the final rings. The hot rolled rings were inspected by ultrasonic testing, of which the results were also validated by metallographic investigation.

In addition to the experimental investigations, coupled thermo-mechanical multi-stage finite element (FE) analysis was performed with integrated adaptive motion control of the rolls. A damage indicator was implemented in a user-defined elasto-viscoplastic material model. The deformations, stresses as well as temperature history from preform forging were included as initial conditions for the rolling stage. Damage indication from the numerical model matches the experimental result in the considered process conditions.

In spite of the suggestion of a more careful process when a low ring growth rate is used in hot ring rolling, experimental and numerical studies demonstrate that with a low ring growth rate there is an increased susceptibility to damage as compared to application of a high ring growth rate.

1. Introduction

Forming a metal above its recrystallization temperature requires much less force and power than cold forming does because of its reduced yield strength and limited strain hardening. The formability and ductility of a metal increase at high temperature. Therefore through hot ring rolling a larger deformation and a wider range of ring cross sections can be achieved than by cold ring rolling. Tiedemann et al. (2007) determine the material flow distribution for radial profile ring rolling. Their investigations on wax-based model material show a high flexibility of the hot ring rolling process.

A typical hot ring rolling process includes preform forging and ring rolling as shown in Fig. 1. The billet is heated to a temperature above the recrystallization temperature of the material. The forming process begins with the upsetting of the hot billet. Next a punch forms a cavity and leaves only a thin web of metal at the hole bottom. In the piercing step, another punch pierces the billet to remove the web of metal. The billet with a complete hole in the center is referred to as preform and is then rolled on a ring rolling mill.

During radial–axial ring rolling, two rolling processes are done simultaneously, radial and axial rolling. In the radial stage, the ring thickness is gradually reduced by reduction of the gap between the main roll and the mandrel (see Fig. 1). The axial stage serves to control the final height of the ring by feeding the upper axial roll towards the lower axial roll. Both processes involve local deformation increments in perpendicular directions which are applied typically between 10 and 100 times to produce one ring. At the same time, the ring cools down at the surface and heats up due to dissipation of heat generated during plastic deformation and friction

* Corresponding author.
E-mail addresses: C.Wang@M2i.nl (C. Wang), H.J.M.Geijselaers@utwente.nl (H.J.M. Geijselaers), Edin.Omerspahic@skf.com (E. Omerspahic), Viktor.Recina@skf.com (V. Recina), A.H.vandenBoogaard@utwente.nl (A.H. van den Boogaard).

http://dx.doi.org/10.1016/j.jmatprotec.2015.08.017
0924-0136/

D_f	final ring outer diameter
σ_v	viscous stress
$\dot{p}$	equivalent plastic strain rate
σ_{eq}	equivalent stress
r	isotropic hardening variable
σ_f	flow stress
p	equivalent plastic strain
T	temperature
σ_0^*	strain and strain-rate independent stress
σ_w	work hardening stress
σ_0	initial yield stress at room temperature
σ_u^*	saturated value of exponential hardening
σ_{u0}	saturated value of exponential hardening at room temperature and at quasi-static threshold rate
C_T	temperature dependence coefficient
C_p	rate dependence coefficient
$\dot{p}_0$	quasi-static threshold rate
p_f	fracture strain
σ_h	hydrostatic stress
Ω	damage indicator
t	time point, current
υ_T	mean velocity of ring at inlet of radial roll gap
S	ring thickness at inlet of radial roll gap
υ_t	mean velocity of ring at outlet of radial roll gap
s	ring thickness at outlet of radial roll gap
υ_H	mean velocity of ring at inlet of axial roll gap
H	ring thickness at inlet of axial roll gap
υ_h	mean velocity of ring at outlet of axial roll gap
h	ring thickness at outlet of axial roll gap
υ_M	tangential velocity of main roll
D_m	mean diameter of ring
υ_A	tangential velocity of axial rolls
L_m	mean circumference of ring
L_i	half mean circumference between inlet of radial roll gap and outlet of axial roll gap
L_o	half mean circumference between outlet of radial roll gap and inlet of axial roll gap
D	outer diameter of ring
υ_r	feed rate of mandrel
t_0	time point, start of ring rolling
s_i	initial ring thickness
V_i	initial ring volume
δs	ring thickness reduction per pass
δh	ring height reduction per pass
υ_a	feed rate of upper axial roll
$\dot{D}$	ring growth rate
Δh_{total}	total ring height reduction
Δs_{total}	total ring thickness reduction
s_f	final ring thickness
h_i	initial ring height
α	opening angle of guide roll arms
D_g	guild roll diameter
R_0	initial ring radius
R	current ring radius
R_a	radius of rotation plane of axial rolls at mean radius of ring
R_m	mean radius of ring
S_x	coordinate of sensor node
υ_x	velocity of sensor node
n_A	rotation speed of axial rolls
n_M	rotation speed of main roll
υ_{Ar}	radial velocity of axial rolls
α_A	semi-vertical angle of conical axial rolls

between ring and rolls. As a consequence, the material experiences a very complex thermo-mechanical deformation history.

An important parameter in the ring rolling process is the ring growth rate, the rate of growth of the ring's outer diameter. The main roll usually rotates at a constant speed throughout the entire process. Therefore, the desired ring growth rate is controlled by the feed rates of the mandrel and the upper axial roll.

While the thickness of the ring is being reduced in the radial stage, simultaneously a slight increase of the height is observed. A similar effect is observed in the axial stage, where height reduction is accompanied with a slight increase in thickness. This phenomenon is referred to as the spread.

The ring rolling process has been subject of a number of experimental and numerical studies. Allwood et al. (2005) describe the development of the ring rolling technology in a thorough literature review. With increasing demand on product life time, optimization of process parameters to improve damage tolerance of the product in service becomes one of the key challenges in ring rolling.

The feed rate is a critical process parameter in the ring rolling process because the relative motions of radial and axial rolls must be controlled to achieve stable rolling, efficient reduction, and accurate final geometry. Many studies have been done to investigate the influence of the feed rate defined rolling schedule on the quality of the final ring. Using slip line theory, Hawkyard et al. (1973) find that in cold ring rolling a sufficiently high feed rate should be applied to avoid tensile stresses in the center of the ring's cross section. Tensile stresses predispose the material to internal cracking. Mamalis et al. (1976) examine the deformation mode of tellurium lead and aluminum alloy rings. They conclude that higher feed rates produce a more rectangular spread. Ryoo et al. (1986) find that as the feed rate increases, the torque of the main roll increases and the force on the mandrel decreases. The influence of feed rate on the mandrel force is less than that on the roll torque. Boucly et al. (1988) simulate the ring rolling with wax-based model materials. From the occurrence of fish tails (uneven spread) it is found that for a certain ring geometry and feed rate of the mandrel, the ratio of radial to axial rolling as well as the rolling curve have to be adjusted. Kluge et al. (1994) develop a new radial–axial rolling strategy to prevent overheating of the spread bulges and to make strain distribution more even. Radial and axial feeding are applied alternately in the proposed rolling schedule. Lin and Zhi (1997) analyze the maximum and minimum feed rates. The minimum feed rate is determined by plastic penetration and the maximum feed rate is determined by bite condition. Yan et al. (2007) propose a mathematical model to plan feed rate for a constant ring growth rate. They conclude that the ring grows uniformly and stably when the ring growth rate is constant. Sun et al. (2008) investigate strain and temperature distribution of the hot rolled ring using a FE model and conclude that a high feed rate improves the strain and temperature uniformity. Sun et al. (2010) analyze the effects of feed rate on micro structural evolution during hot ring rolling of AISI 5140 steel by a FE model. They show that increase of feed rate enlarges the regions of recrystallization. In addition, the distribution of recrystallization becomes more uniform. Zhou et al. (2011) study forming defects in hot rolling of aluminum alloy using FE simulation and find that a high ratio of axial to radial feed per revolution leads to less uniform deformation.

Under some process conditions defects such as porosity can be found in rings produced from high alloyed steels. High alloyed steel ingots tend to contain macro segregations (Campbell, 2003). In none of the aforementioned studies on the effect of feed rate, its influence on damage development in the bulk of the ring has been subject of investigation.

In this work the influence of ring growth rate on the occurrence of macro defects in the bulk of the ring is studied. Billets were hot forged and then ring rolled with different feed rate programs,

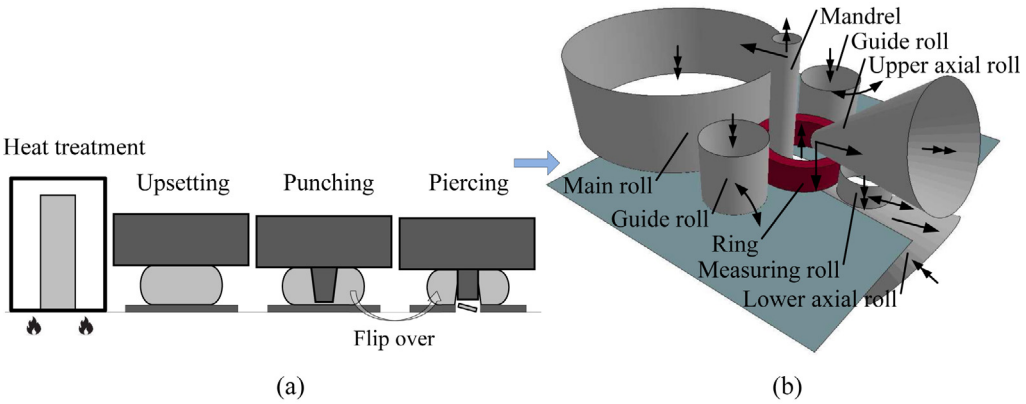

Fig. 1. Process chain of hot ring rolling: (a) preform forging and (b) ring rolling.

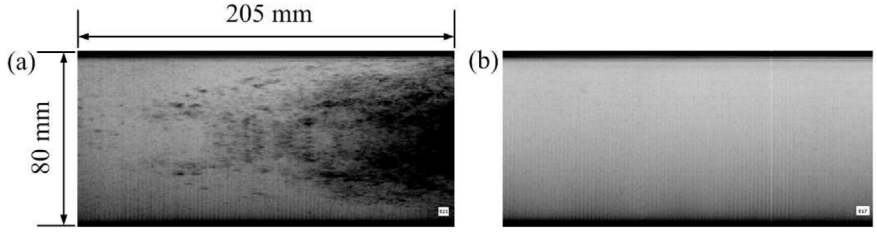

Fig. 2. Ultrasonic testing images of (a) a bar having strong porosity indications and (b) a bar appearing healthy.

which are determined by specification of different desired constant ring growth rates. The porosity (damage) in the final rings, was identified with the help of ultrasonic inspection. Additionally the influence of ring growth rate is investigated numerically to explain the experimental results.

2. Test design

The tests were designed for the purpose of investigating the effect of the ring growth rate on final quality of the rolled rings. For the ring rolling stage, three different conditions were prescribed with respect to the feed rate program of the mandrel and the upper axial roll.

2.1. Sample selection

The steel used in this research is AISI 52100 type alloy. One of the inevitable sources of damage in metal forming processes is the existence of defects in the billet material. Campbell (2003) describes that casting ingots usually have macro-porosity and macro-segregation as two major defects. A macro-porosity is either a gas entrapment or a void in the casting product, which is big enough to be detected by ultrasonic inspection. Macro-segregation is a spatially uneven distribution of alloying elements due to solidification during casting.

For the tests, steel billets were first cut from the ingots near the segregation area (center section) of the chosen ingot. Next, round bars of 80 mm in diameter and 205 mm in height were machined out of the center line of the billets. All the bars were then inspected by ultrasonic testing so as to identify the initial quality of the samples. A great difference in terms of indications that are signs of macro-porosity and non-metallic inclusions was observed in ultrasonic testing imaging. An impression of billets with weak and strong indications is given in Fig. 2. The samples for the tests were selected from the billets in which no macro-porosity was identified.

Table 1
General dimensions after each operation.

	Height (mm)	Outer diameter (mm)	Ring thickness (mm)
Billet	205.0	80.0	–
Upsetting	83.0	125.7	–
Punching	83.0	133.1	40.6
Ring rolling	50.0	405.4	16.0

2.2. Test conditions

The selected samples were used to manufacture rings on a ring rolling machine. The tests included all operations as in a typical hot ring rolling production system involving heat treatment and machining. The dimensions of the billet, preform and final ring are given in Table 1.

The initial hot working temperature is set to $T = 1150\,^{\circ}C$. The temperatures were recorded by an infrared camera in order to know the temperature history and its distribution on the workpiece.

Three feed rate programs had to be determined in advance by specification of three constant ring growth rates as the inputs for the tests and simulations. A high, an intermediate and a low ring growth rate are considered. The radial–axial ring rolling involves two roll gaps. The rotational and translational motions of both roll pairs are related. Koppers and Kopp (1991) derive analytical equations for the geometry and kinematics of the radial–axial ring rolling process. The adaptive control model, which they developed, has been successfully adopted in industrial rolling mills. Yan et al. (2007) describe a mathematical relationship between the ring growth rate and the feed rate of the mandrel in radial ring rolling. For this study an analytical model, used in conjunction with adaptive motion control of the rolls, was built to determine the feed rate program in the radial–axial ring rolling process (see Appendices A and B). Assigning process conditions (see Section 2.2) to Eq. (A.21) and specifying a linear relation in Eq. (A.20), the feed rate programs can be determined for the three

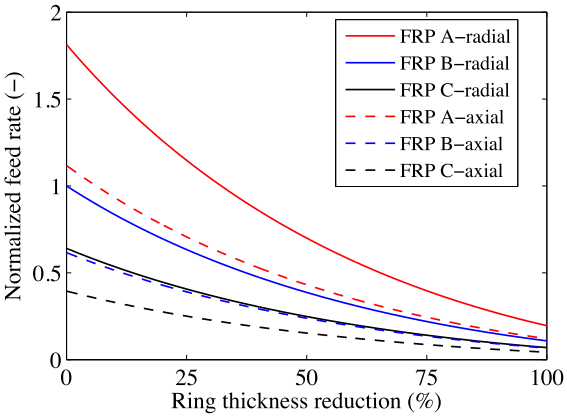

Fig. 3. Feed rate programs.

considered ring growth rates. In Fig. 3 the feed rates of the mandrel and of the upper axial roll, as functions of the actual ring thickness reduction, are plotted for a high feed rate program (FRP A), an intermediate feed rate program (FRP B) and a low feed rate program (FRP C).

2.3. Ultrasonic testing of final rings

After cooling, the rings were finely ground to increase the precision of the ultrasonic testing. The ultrasonic immersion method was used for the detection of subsurface defects. The rolled ring was carefully centered and mounted on a rotating table before being sunk in the immersion tank. The automated scanning was performed with an immersion transducer, which has a center frequency of 10 MHz and crystal diameter of 19 mm. The transducer was focused spherically on a 145 mm spot in water and its position was adjusted by a servo-motor's integrated motion controller. Fig. 4 shows schematically the ultrasonic testing set-up. The 45° refracted shear wave in steel was produced to visualize the results. The circumferential and axial resolution are 0.3 mm and 0.2 mm respectively.

3. Finite element analysis

A coupled thermo-mechanical multi-stage FE model was built in the commercial code LS-DYNA to simulate the preform forging and the ring rolling. Explicit time integration is used for mechanical calculations and implicit time integration is used for thermal calculations. Both solvers are connected in a staggered solution scheme. A damage indicator is implemented in a user-defined material model with temperature dependence.

3.1. Material model

The preform forging as well as the ring rolling are executed at high operating temperatures. To model the strain rate dependence of the material response, an elasto-viscoplastic von Mises material model is used.

3.1.1. Viscoplasticity

An over-stress type viscoplasticity model was chosen. The viscous stress, σ_v, contains a dependence on the equivalent plastic strain rate $\dot{p}$. Moreover, $\dot{p}$, the plastic multiplier for a von Mises material, is determined through the use of a viscoplastic constitutive equation as opposed to being determined by the consistency condition:

$$\dot{p} = \psi(\sigma_{eq}, r), \tag{1}$$

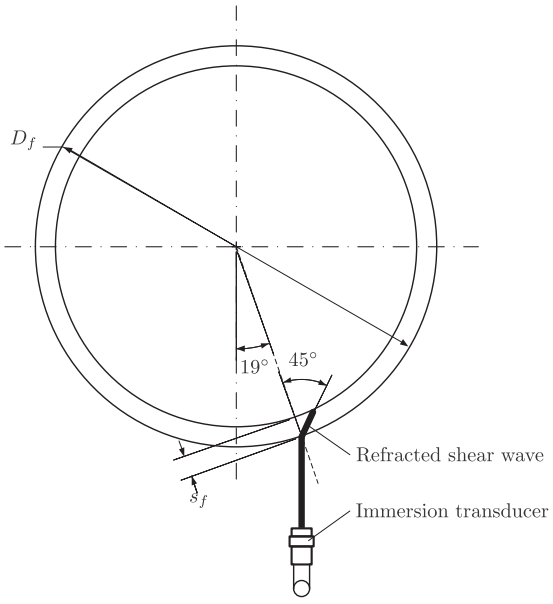

Fig. 4. Sketch of the ultrasonic testing set-up.

where σ_{eq} is the (von Mises) equivalent stress and r is the isotropic hardening variable. This is described in Dunne and Petrinic (2005).

3.1.2. Flow stress

The flow stress σ_f is a measure of the resistance to (further) plastic deformation of a material. Experiments performed in advance at operating temperatures of hot ring rolling, show that the flow stress in AISI 52100 type alloy depends on the temperature and strain rate. In this study, the flow stress is defined as a function of equivalent plastic strain p, equivalent plastic strain rate $\dot{p}$ and temperature T. The model starts with a decomposition of σ_f into a temperature dependent yield stress σ_0, a work hardening term σ_w and a viscous stress σ_v:

$$\sigma_f = \sigma_0^*(T) + \sigma_w(p, \dot{p}, T) + \sigma_v(\dot{p}). \tag{2}$$

Apart from the viscous stress (see Fig. 5), the effect of strain rate on work hardening is also included to be able to describe the experimental observations (see Fig. 5).

The yield stress σ_0^* is expressed as

$$\sigma_0^* = \sigma_0 C_{T,1}, \tag{3}$$

where σ_0 is the initial yield stress at room temperature and $C_{T,1}$ is the temperature dependent coefficient.

The work hardening part σ_w is described by a double exponential (Voce) hardening, as

$$\sigma_w = \sigma_{u1}^*(1 - \exp(-m_1 p)) + \sigma_{u2}^*(1 - \exp(-m_2 p)), \tag{4a}$$

with

$$\sigma_{u1}^* = \sigma_{u0} C_{T,2} C_{p,1}, \tag{4b}$$

$$\sigma_{u2}^* = \sigma_{u0} C_{T,3} C_{p,2}, \tag{4c}$$

where $m_{:s}$ are the material parameters of Voce hardening, $\sigma_{u:s}^*$ is the saturated values of exponential hardening, σ_{u0} is the saturated value of exponential hardening at room temperature and at quasi-static threshold rate, $C_{T,:s}$ is the temperature dependent coefficients, and $C_{p,:s}$ is the strain rate dependent coefficients.

Finally, the viscous stress σ_v has to be determined. Knowing Eqs. (1) and (2), σ_v is then formulated by the inverse of function ψ

$$\dot{p} = \psi(\sigma_v) = \psi(\sigma_{eq} - \sigma_w - \sigma_0^*) = \alpha \sinh \beta(\sigma_{eq} - \sigma_w - \sigma_0^*), \tag{5}$$

where α and β are material parameters.

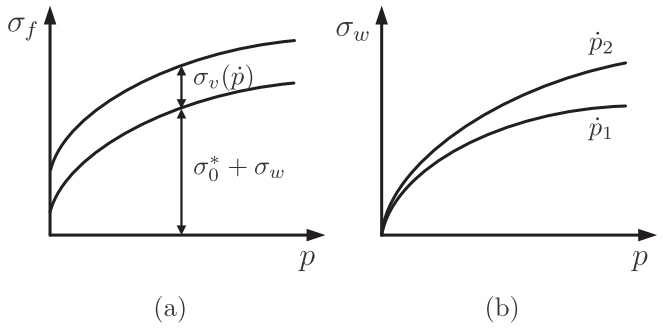

Fig. 5. Strain rate dependence of (a) viscous stress and (b) work hardening.

Consequently

$$\sigma_v = \Psi(\dot{p}) = \frac{1}{\beta} \ln \left(\frac{\dot{p}}{\alpha} + \sqrt[2]{\left(\frac{\dot{p}}{\alpha}\right)^2 + 1} \right), \tag{6}$$

The temperature and strain rate dependent terms in above equations are defined as follows:

$$C_{T,i} = \exp\left(-a_i \frac{T - T_0}{T_m}\right), \quad i = \{1, 2, 3\}, \tag{7}$$

$$C_{p,j} = 1 + b_j \ln\left(\frac{\dot{p}}{\dot{p}_0}\right) + d_j \left(\ln \frac{\dot{p}}{\dot{p}_0}\right)^2, \quad j = \{1, 2\}, \tag{8a}$$

where the equivalent plastic strain rate normalized by the quasi-static threshold rate $\dot{p}_0$ and a_i, b_j and d_j are material parameters.

Although some of the material parameters of this model can be determined beforehand, the majority of them have been obtained by fitting experimental results of 12 hot compression tests (4 strain rates and 3 different temperatures). In Fig. 6a comparison between the experimental and the fitted numerical true stress-strain curves can be seen. The strain rates in the deformation zones of ring rolling reach values up to 20 s^{-1}.

3.1.3. Damage indicator

Damage is the progressive mechanical degradation leading to macroscopic fracture. In case of ductile metallic materials, fracture consists of three stages:

- Initiation of cavities by breaking interface bonds.
- Growth of cavities up to a critical dimension.
- Coalescence of these cavities leading to the final rupture.

The damage is modeled by an uncoupled model, in which the damage has no influence on the stress–strain relation. Porosity is a fraction of the volume of voids over the total volume. Density of the material decreases when porosity increases. The volumetric strain can thus be a good measure for describing ductile fracture. From the equations from plasticity theory for porous materials Oyane et al. (1980) derive a criterion for the ductile fracture of pore-free materials as

$$\int_0^{p_f} \left(1 + \frac{\sigma_h}{A\sigma_{eq}}\right) \mathrm{d}p = C, \tag{9}$$

where σ_h is the hydrostatic stress, p_f is the fracture strain and C is the critical damage value. Parameters A, and C are material constants to be determined from experimental measurements when fracture is observed. This criterion provides satisfactory result for upsetting with open dies. Metal materials are sensitive to hydrostatic tension when micro voids are present. Comprising Oyane's method to account for triaxiality, an evolution equation for the damage indicator Ω based on the plastic strain, is proposed in this work as

$$\mathrm{d}\Omega = \frac{\langle\sigma_h\rangle}{\sigma_{eq}} \mathrm{d}p, \tag{10a}$$

with

$$\langle\sigma_h\rangle = \frac{1}{2}(\sigma_h + |\sigma_h|), \tag{10b}$$

Only the hydrostatic tension is assumed to contribute to the damage indicator.

The computed indicator value is only intended for comparison between different process conditions. A critical damage value will not be defined.

3.1.4. Implementation into LS-DYNA

The aforementioned model is written in a FORTRAN subroutine that is called by the LS-DYNA user material interface. Based on the actual temperature calculated by the implicit thermal solver, the temperature dependent constitutive material properties are calculated in the explicit mechanical solver. The plasticity constitutive equations are fully integrated for finite increments of strain. The Newton–Raphson method is used to determine the equivalent plastic strain increment iteratively. The damage indicator is updated at the end of each time increment.

The ring undergoes large rotations in the ring rolling process. Second order objective stress updates are thus necessary here despite employing the explicit time integration scheme with small time steps. The Jaumann rate equation is used and the strain–displacement matrix is computed at the mid-point configuration. The local material coordinate system is invoked for the material routines.

3.2. FE simulation of preform forging and 2D to 3D mapping

Simulations of the preform forging stages (upsetting, punching and piercing) are carried out by 2D axisymmetric model with high mesh density. Adaptive remeshing is applied to avoid element distortion and small characteristic element size is controlled to achieve good results. The element erosion technique is employed in the piercing step to punch out the web of metal, left after the punching step, as shown in Fig. 1a. The details can be found in Wang et al. (2013).

After the preform forging, the cooling during the transport from the preform forging station to the ring rolling mill is also considered by the thermal solver. The convection boundary condition is simulated by using a temperature dependent heat transfer coefficient.

The results of the 2D preform forging simulation are mapped to a target 2D mesh tailored for simulation of the rolling stage. A 3D preform is then obtained by sweeping the 2D cross section. All the stresses, strains, damage, state variables and temperatures are mapped onto the 3D solid elements.

3.3. FE simulation of ring rolling

The ring rolling model built in this study contains all the parts as shown in Fig. 1b. The complete billet height is modeled, the support plane and gravity are also taken into consideration. Water cooling is applied to the rolls of the rolling mill. Therefore, it is assumed that the rolls keep their initial temperature (25 °C). The ring temperature changes due to the thermal contact with the rolls. Heat generation from plastic work and heat generated by sliding friction are included in the thermal calculations. The maximum friction force is limited by the shear strength of the material. For a detailed prediction of the damage level and an adequate

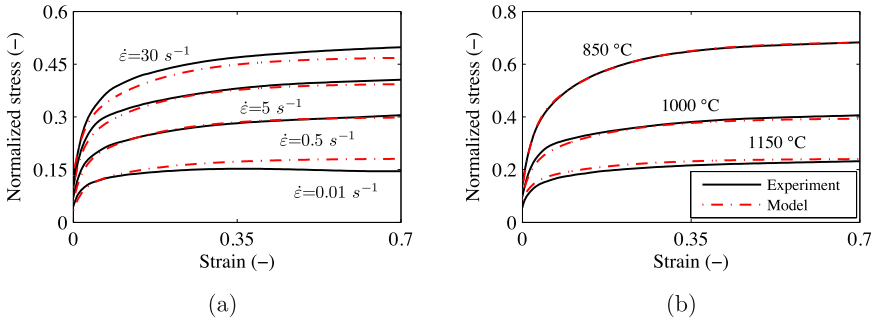

Fig. 6. Calibrated numerical true stress–strain curves compared to experimental ones: (a) T = 1000 °C and (b) $\dot{\varepsilon} = 5\,s^{-1}$.

description of the profile filling behavior, the ring is finely meshed with 170,640 solid elements (8-noded hexahedron with reduced integration).

3.3.1. Time stepping in a staggered solution scheme

The critical implicit thermal time step is usually some orders of magnitude larger than the critical explicit mechanical time step. However, in a staggered solution scheme the thermal time step has to be small enough to capture the mechanical motion. In this work, automatic time stepping is used for the thermal solver by defining a proper maximum allowed temperature change per step, which requires a preliminary study on convergence. For the mechanical time step, the selective mass scaling implemented in LS-DYNA is invoked for the ring. In many processes the energy content in the high frequency domain is much smaller than that in the low frequency domain. Olovsson et al. (2005) propose methods that add artificial mass on high frequency domain to increase the critical time step without significantly affecting the low frequency behavior. This approach, referred to as selective mass scaling, optimizes computational efficiency of the explicit simulation of the ring rolling process effectively, on account of the high rotation speed of the ring and a small volume fraction of the plastic deformation zones. No additional stress due to rotational inertia is introduced.

3.3.2. Adaptive motion control

This FE model is dedicated to delivering simulations of the hot ring rolling process with a desired constant ring growth rate by adaptive control of the rolls' motion. Bulging is observed after preform forging (see Fig. 7). The cross section of the preform has an irregular shape instead of being rectangular. The ring outer diameter decreases slightly at the initial rolling stage because the material flows to the unconstrained spaces, as mentioned in Wang et al. (2013). Therefore, in this model, the control algorithm has two stages to take the irregular preform shape into account. In the first stage, the initial feed rate of the radial feeding curve in Fig. 3 (see Section 2.2) is applied for the mandrel while the upper axial roll holds its axial position. The second stage (main stage) begins when the rectangular cross section is reached.

An explicit expression of the function in Eq. (A.21) is generated for $\upsilon_r(t)$ off-line. This expression is then written in a FORTRAN subroutine and implemented in the FE model. The feed rates of the mandrel $\upsilon_r(t)$ and of the upper axial roll $\upsilon_a(t)$, are then adaptively controlled as function of the actual ring thickness $s(t)$, which results from the simulation response (see Appendix A). As mentioned in Section 2.2, the control model of the feed rate program functions in conjunction with the adaptive motion control of the rolls (see Appendix B).

4. Results

4.1. Simulation results of preform forging

FE modeling of plastic forming processes provides increased process understanding as the distribution of stress, strain and temperature can be examined. Fig. 7 shows the temperature distribution, the equivalent plastic strain distribution and the damage indication after the preform forging simulation. The temperature distribution shown here was obtained after simulation of transport from the preform forging station to the ring rolling mill. In Fig. 7a, the chilling effect due to the contact with the cold punch is still visible. The large strain region is located in the inner side of the billet where the punching and piercing happen, as shown in Fig. 7b. Fig. 7c shows that relatively high damage value is indicated at the onset of fracture zone during the piercing process. In the bulging area there is an area of high damage due to the action of the conical punch.

4.2. Ring rolling simulation results

Fig. 8 shows the temperature distribution and the equivalent plastic strain distribution in the virtually rolled ring. The ring is warmer in the center of the cross section and colder on the surface due to the contacts with cold tooling. The outer ring surface is heated by friction from the main roll while the inner surface is cooled by the idle mandrel. High strain peaks are observed in the cross section's corners due to the constant formation and deformation of the spread bulges in the radial–axial ring rolling. This portion of material is normally milled away.

To obtain accurate results on temperature dependent constitutive material properties in this coupled thermo-mechanical analysis, it is crucial to predict an accurate temperature distribution in the simulation. The thermal material properties, like heat capacity and thermal conductivity, were taken from the data sheet of the material provider. However, for the heat transfer coefficient no reliable values are available. In this study, trial simulations were first performed with a range of thermal coefficients. Then those coefficients were calibrated by comparing the temperature distribution to the experimental references, which are infrared images captured during the tests. The heat transfer coefficients used for the different contact pairs (between the ring workpiece and the tooling) are listed in Table 2.

Under the premise of convergence, larger time steps should be used for computational efficiency in the implicit thermal solver. However, as mentioned in Section 3.3.1, for a staggered solution scheme of this model the thermal time step has to be small enough to capture the mechanical motion. It should thus be noted that the ratio of thermal to mechanical time step has to be controlled within a critical value when automatic time stepping is adopted. In this study, it is recommended to limit the ratio to 20. This gave rise

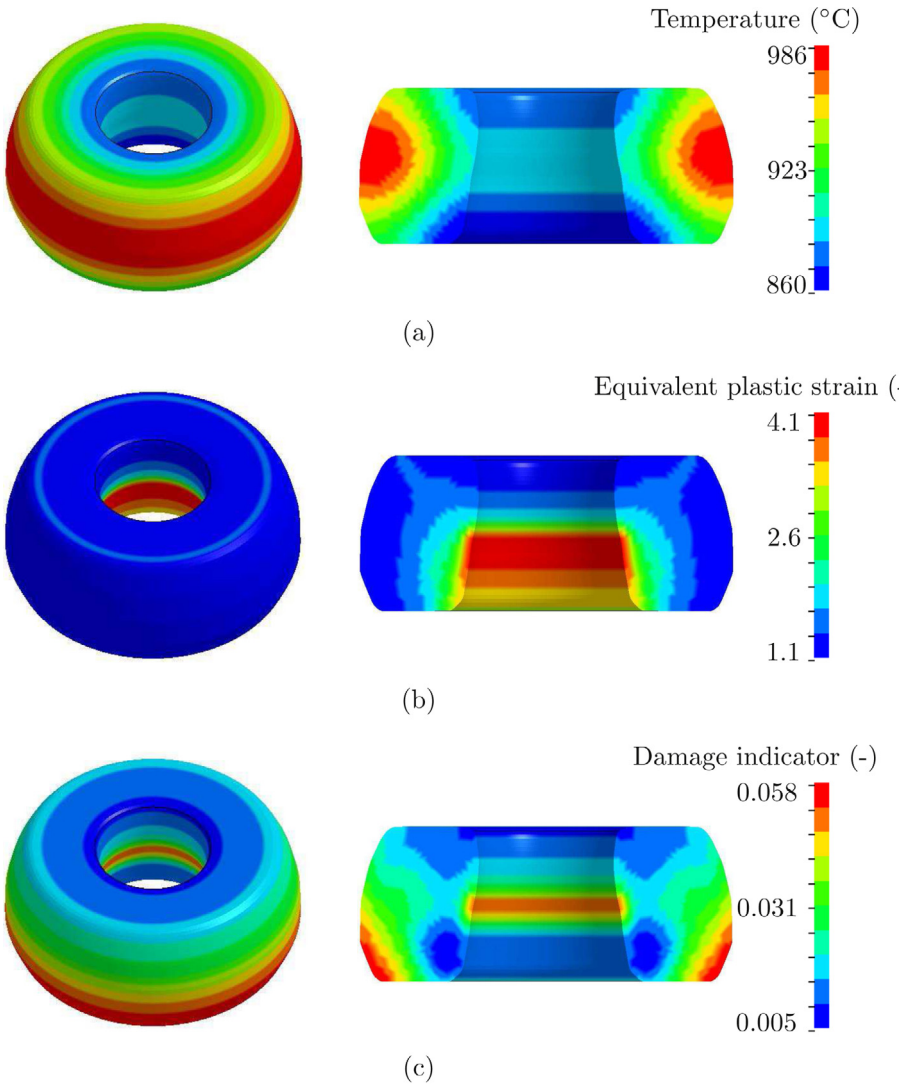

Fig. 7. Contour plots of (a) temperature, (b) equivalent plastic strain and (c) damage indicator in the preform.

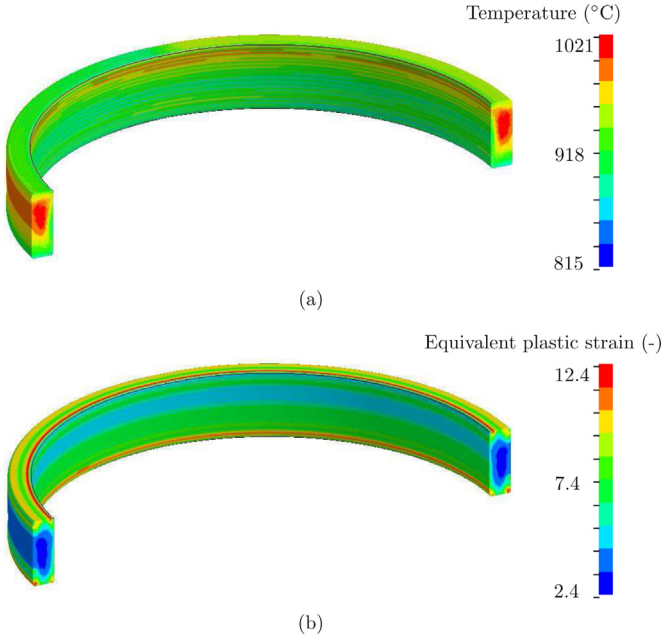

Fig. 8. Contour plots of (a) temperature and (b) equivalent plastic strain in the ring.

Table 2
Heat transfer coefficients between the ring workpiece and the tooling.

Tooling in contact	Heat transfer coefficients (kW/m^2 K)
Main roll	6.0
Mandrel	6.0
Axial rolls	18.0
Support plane	1.0

to the computational time of approximately 80 h on 24 processors (Intel(r) Xeon(r) CPU X5650@2.67GHz), performed with the MPP (massively parallel processing) execution of a single ring rolling simulation.

4.3. Results of damage indication from experiment and simulation

Ultrasonic immersion scanning was used for detection of defects. Both the ring and the ultrasonic transducer were submerged in water and the entire ring volume was inspected by automated scanning. The images from ultrasonic scanning indicate whether any defects are present in the ring. The equipment shows the peak response within the time or depth interval of interest as a function of the transducer position. Any discontinuity is indicated in the image with different gray scale compared to the base material. The defects are presented as dark areas on a lightly gray colored background.

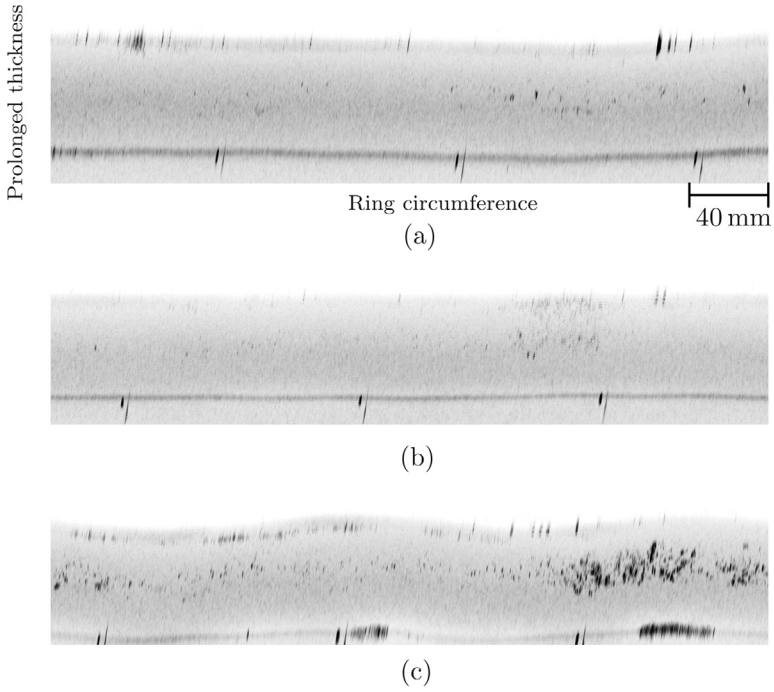

Fig. 9. Ultrasonic testing images of rings rolled with (a) feed rate program A, (b) feed rate program B and (c) feed rate program C.

Fig. 9 shows the ultrasonic testing results of the rolled rings from performed experiments. The short edge of the image is the prolonged thickness of a ring which is the real wall thickness corrected for the refraction angle of the ultrasonic testing, while the long edge represents the ring circumference. From these images, it can be observed that the FRP C with the low ring growth rate developed considerable macro voids that are concentrated around the center of the ring thickness. In contrast, the FRP A and FRP B with a high and an intermediate ring growth rate, display low amounts of macro voids. No macro voids were observed in the billets of any of the rings (see Section 2.1).

To validate the output from the ultrasonic testing, metallographic investigation of critical ring sections (dark areas) has been performed subsequently. Specimens for the inspection were sectioned from the rolled rings and examined by light microscope. Fig. 10 shows the results of a specimen made in transverse direction for the ring rolled with FRP C. Several clusters of voids located in near proximity (Fig. 10a) show the characteristic distribution pattern of voids in the ring. Fig. 10b shows the voids detected in the zoomed-in image.

In addition, mapping of the voids distribution in the transverse direction has been performed using the *x*–*y* table on the light optical microscope. Fig. 11 shows that the voids in the ring rolled with the low ring growth rate are located around the center of the examined cross section. The distribution corresponds to the location of defects in the ultrasonic image (see Fig. 9c). Two different cross sections were investigated.

For the simulation results, the nodal values of damage indicator and the nodal coordinates have been extracted to generate the damage indication map as shown in Fig. 12. The intention of this post-processing is to reproduce a damage inspection image similar to the one from ultrasonic testing. The *x*-axis on those images is the circumferential coordinate and the *y*-axis is the normalized wall thickness. The domain of a ring is then divided into a number of boxes in circumferential and radial direction. Each box represents a bulk volume of that ring. The gray scale indicates the logarithmic mean damage indicator value of each box. The darker color represents stronger damage indication, similarly to the representation in the ultrasonic testing images. The values of 0.1–0.9 (0–1 equals the entire ring thickness) in the y-axis mean that regions at most inner

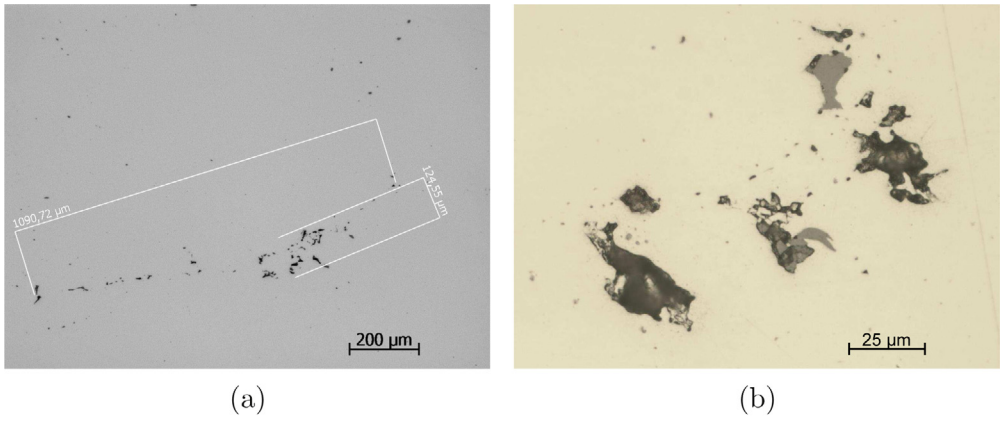

Fig. 10. Microscope images of specimen from ring rolled with low ring growth rate: (a) overview showing several clusters of voids and (b) voids in zoomed-in image.

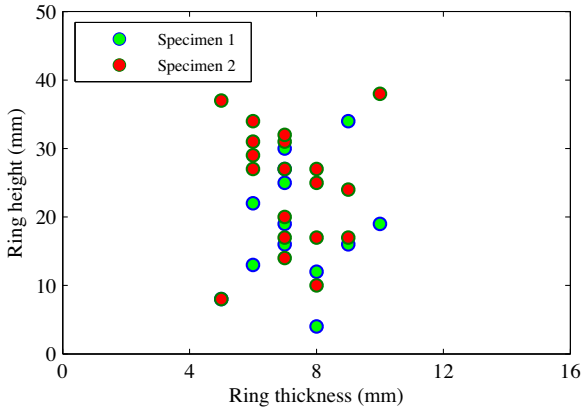

Fig. 11. Voids distribution chart (FRP C).

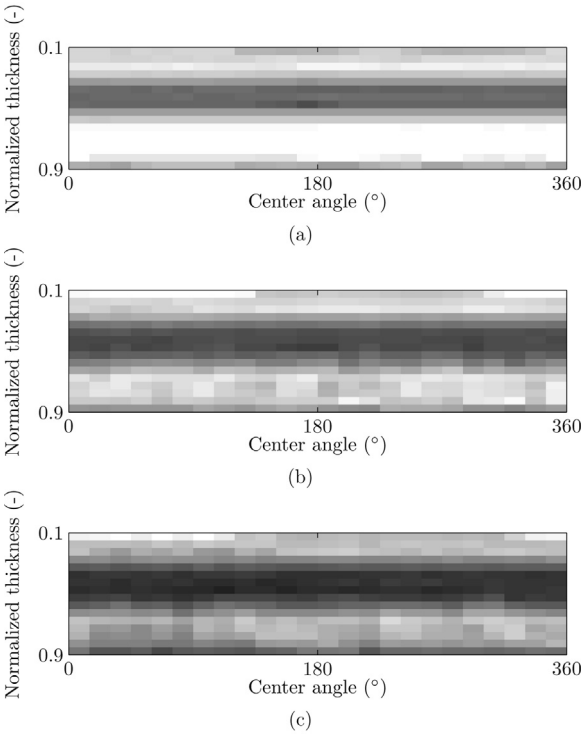

Fig. 12. Damage indication from rings simulated with (a) high ring growth rate, (b) intermediate ring growth rate and (c) low ring growth rate.

and outer surfaces are excluded to avoid the effects of repetitive formation and deformation of spread bulges.

Similarly to the experimental observations, FE simulations for the FRP C, with the low ring growth rate, indicate the highest damage values concentrated around the center of the ring thickness.

5. Discussion

The formulation of the damage indicator (see Section 3.1.3) implies that the low ring growth rate leads to a triaxial tensile stress state in the center of the ring. Therefore, macro voids are formed by the coalescence of neighboring micro voids. Fig. 13 illustrates the cross-sectional distribution of positive stress triaxiality when ring thickness reduction has reached 20%. High positive stress triaxialities are observed in the simulations with the low ring growth rate (Fig. 13b).

Hawkyard et al. (1973) describe that a triaxial tensile system exists in the central section of the ring when the ratio of current

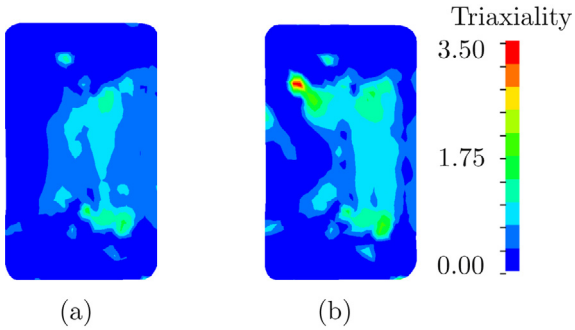

Fig. 13. Contour plots of stress triaxiality in ring cross section after 20% reduction: (a) high ring growth rate and (b) low ring growth rate.

ring thickness to roll contact length is larger than 4.85. To avoid this condition it would be necessary to roll at a high feed rate to ensure that the ratio is smaller. This ratio was also calculated from the FE simulations in this study. The highest value, 4.38, was found in the simulations with the low ring growth rate (FRP C). For the simulations with the intermediate ring growth rate (FRP B) and the high ring growth rate (FRP A), they are 4.13 and 3.87, respectively. It appears that the criterion by Hawkyard et al. is not conservative for this study. Moreover, it is not very discriminate.

Specification of a low ring growth rate during ring rolling will promote generation of defects in the bulk of the ring. The reason for this is that the low feed rate associated with a low ring growth rate causes only superficial plastic deformation of the rolled surfaces. The bulk of the ring is forced to stretch in a state of tensile stress. This effect is also known in cold rolling of sheet metal where a final 'skin pass' is often applied to induce compressive stresses in the sheet's skin. A second effect of applying a low feed rate is that the ring cross section is submitted to more deformation passes compared to rolling with a high feed rate. The high number of tensile stress cycles apparently causes nucleation and growth of voids in the center of the ring cross section.

Moreover, application of a high feed rate causes more uniform deformation of the ring cross section. The spread is more 'rectangular'. As a consequence the ring surface is subjected to less severe deformations with fewer cycles. The surface quality is better and less material has to be milled away.

6. Conclusion

A coupled thermo-mechanical multi-stage FE model has been built in the commercial FE code LS-DYNA to simulate the hot ring rolling process including the preform forging. A user-defined viscoplastic material model has been implemented. An uncoupled damage indicator has been included to evaluate the chance of generating porosity (damage) during the ring manufacturing process. The ring rolling simulations have been carried out with integration of a control algorithm using simulation response data.

The FE simulations have been performed with process settings identical to the experiments. The selected samples have been forged and hot ring rolled with different feed rate programs. These feeding scenarios have been recreated by the analytical control mentioned above (with desired ring growth rates). Different feeding rates were supposed to give different amounts of porosity (damage) in the manufactured rings.

The billets and the rolled rings have been inspected by ultrasonic testing to identify the damage levels. The ultrasonic testing results have been subsequently validated by the metallographic investigations. The damage results indicated in the simulations match the experimental results well for the presented process conditions.

Together, they reveal the hidden danger of inappropriate low ring growth rate in the process of hot ring rolling.

Acknowledgements

This research was carried out under the project number M41.1.11418 in the framework of the Research Program of the Materials innovation institute M2i (www.m2i.nl). The industrial partner, SKF Group is gratefully acknowledged for the contributions to this research.

Appendix A. Kinematics of ring rolling

The geometry and kinematics of radial–axial ring rolling, which are being considered in this model is illustrated in Fig. A.1. The shaded regions in the figure represent the deformation zones. All quantities are assumed to be given at current time t, unless indicated otherwise.

Some assumptions are made in this study to simplify the model. The cross section of the ring is rectangular and the spread of the two unrestrained sides of the cross section is neglected in both radial and axial roll gaps. In Fig. A.1a, υ_T and S are the mean velocity of the ring and the ring thickness at the inlet of the radial roll gap, respectively. Correspondingly, υ_t and s are the mean velocity of the ring and the ring thickness at the outlet of the radial roll gap. The continuity of metal flow in the roll gap gives

$$\upsilon_T = \frac{s}{S}\upsilon_t, \tag{A.1}$$

$$\upsilon_H = \frac{h}{H}\upsilon_h, \tag{A.2}$$

where υ_H and H are respectively the mean velocity of the ring and the ring height at the inlet, υ_h and h are the mean velocity of the ring and the ring height at the outlet, respectively. The tangential velocity at the outer diameter of the ring at the outlet of the radial roll gap is equal to the tangential velocity of the main roll υ_M, if it is assumed that slip between the main roll and the ring can be neglected. By assuming also that the velocity distribution is linear along the radial roll gap, the geometry in Fig. A.1a indicates that υ_t is proportional to the velocity at the outer diameter:

$$\upsilon_t = \frac{D_m}{D_m + s}\upsilon_M, \tag{A.3}$$

where D_m is the mean diameter of the ring.

Likewise, for no slip

$$\upsilon_h = \upsilon_A, \tag{A.4}$$

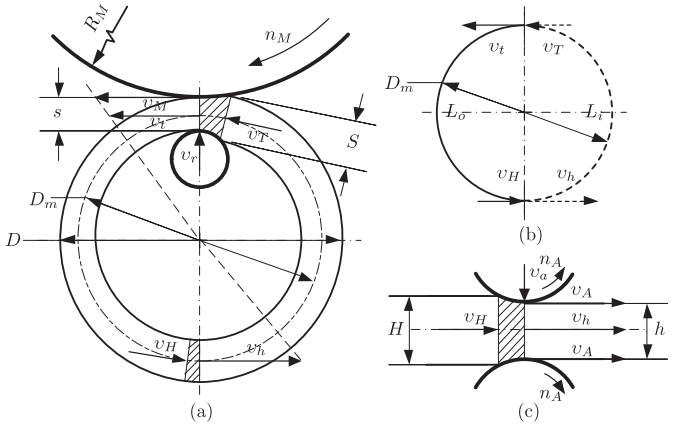

Fig. A.1. Assumed geometry and kinematics of radial–axial ring rolling: (a) top view, (b) segmentation of ring's mean circumference and (c) radial view at axial roll gap.

where υ_A is the tangential velocity of the axial rolls. As shown in Fig. A.1b, the two roll gaps partition the mean circumference of the ring L_m into two sections, i.e., the half between the inlet of the radial roll gap and the outlet of the axial roll gap L_i, and the other half between the inlet of the axial roll gap and the outlet of the radial roll gap L_o. The ring enlargement can then be formulated by the changes of the mean velocities:

$$\pi\dot{D}_m = \dot{L}_m = \dot{L}_i + \dot{L}_o \tag{A.5a}$$

with

$$\dot{L}_i = \upsilon_h - \upsilon_T, \tag{A.5b}$$

$$\dot{L}_o = \upsilon_t - \upsilon_H. \tag{A.5c}$$

From the requirement that the ring must always grow symmetrically to the rolling mill's axis, i.e., the symmetry condition, the equality of the growth rate of the ring between two sections is inevitable:

$$\upsilon_h - \upsilon_T = \upsilon_t - \upsilon_H \tag{A.6}$$

Combining this with Eqs. (A.1) and (A.2) gives

$$\upsilon_h = \frac{H(S+s)}{S(H+h)}\upsilon_t. \tag{A.7}$$

This prerequisite of the symmetry condition is satisfied when velocities from Eq. (A.4) become known, by controlling the rotation speed of axial rolls. This is introduced later in Appendix B. On account of the small reduction per pass, the outer diameter of the ring

$$D = D_m + s. \tag{A.8}$$

A relationship between current ring thickness s and the feed rate of the mandrel υ_r can be obtained as

$$s = s_i - \int_{t_0}^{t} \upsilon_r(\tau)\,\mathrm{d}\tau. \tag{A.9}$$

Deriving Eq. (A.8) and using Eq. (A.9), as done by Yan et al. (2007), then gives

$$\dot{D}_m = \dot{D} + \upsilon_r. \tag{A.10}$$

Substituting Eqs. (A.2), (A.6) and (A.10) into Eqs. (A.5a), (A.5b) and (A.5c) gives

$$\pi(\dot{D} + \upsilon_r) = 2\left(\upsilon_t - \frac{h}{H}\upsilon_h\right). \tag{A.11}$$

Combining this with Eqs. (A.3), (A.7) and (A.8), gives

$$\dot{D} = \frac{2\upsilon_M(D-s)}{\pi D}\left(1 - \frac{h\left(2s+\delta s\right)}{\left(s+\delta s\right)\left(2h+\delta h\right)}\right) - \upsilon_r, \tag{A.12a}$$

with

$$\delta s = S - s, \tag{A.12b}$$

$$\delta h = H - h, \tag{A.12c}$$

where D can also be related to s, h and the initial volume of the ring V_i as

$$D = \frac{V_i}{\pi h s} + s. \tag{A.13}$$

If it is assumed that slip between the main roll and the ring can be neglected, a relationship between the ring thickness reduction in the radial roll gap per pass, δs, and the feed rate of the mandrel υ_r is obtained in Hawkyard et al. (1973) as

$$\delta s = \frac{\pi D}{\upsilon_M}\upsilon_r. \tag{A.14}$$

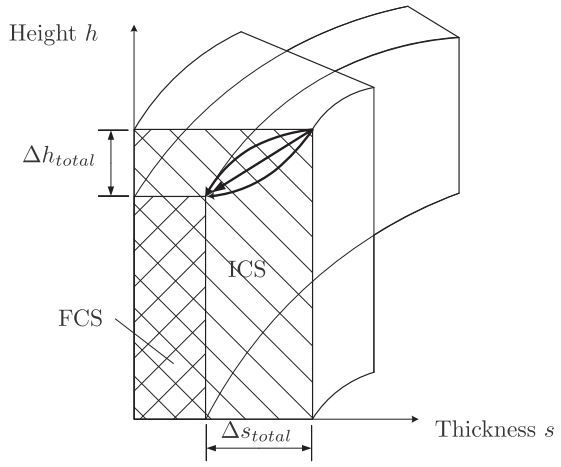

Fig. A.2. Rolling curves.

Similarly, a relationship between the ring height reduction in the axial roll gap per pass, δh, and the feed rate of the upper axial roll υ_a is

$$\delta h = \frac{\pi D}{\upsilon_M}\upsilon_a. \tag{A.15}$$

The tangential velocity of the main roll υ_M is known when the main roll rotates at a constant speed n_M, as mentioned in the introduction. Ring growth rate $\dot{D}$ can then be related to s, h, υ_r and υ_a by combining Eqs. (A.12a), (A.12b), (A.12c), (A.13), (A.14) and (A.15), giving

$$\dot{D} = f(s, h, \upsilon_r, \upsilon_a, V_i). \tag{A.16}$$

Once the loading path is designed, a certain rolling curve is determined. Fig. A.2 shows schematically that the different rolling curves can be selected for the same ring geometry. The initial cross section (ICS) is squeezed into the final cross section (FCS) by the pressure rolls, with a total ring thickness reduction Δs_{total} and a total ring height reduction Δh_{total}.

When a certain rolling curve is selected, the ring height h can be expressed as a function of ring thickness s, giving $h = g(s)$, $s \in [s_i, s_f]$. Calculating the time derivative of h, gives

$$\dot{h} = \frac{\mathrm{d}h}{\mathrm{d}t} = \frac{\mathrm{d}g(s)}{\mathrm{d}s}\frac{\mathrm{d}s}{\mathrm{d}t} = g'(s)\dot{s}, \tag{A.17}$$

where $g'(s)$ is the derivative with respect to s. Similarly to Eq. (A.9), the current ring height h can be related to the feed rate of the upper axial roll υ_a by

$$h = h_i - \int_{t_0}^{t} \upsilon_a(\tau)\,\mathrm{d}\tau, \tag{A.18}$$

where h_i is the initial ring height. Calculating the time derivatives yields

$$\dot{s} = -\upsilon_r, \tag{A.19a}$$

$$\dot{h} = -\upsilon_a. \tag{A.19b}$$

Combining these relationships and Eq. (A.17), υ_a can then be related to υ_r as

$$\upsilon_a = g'(s)\upsilon_r. \tag{A.20}$$

It is now possible to define υ_r as a function of ring thickness s, ring height h, ring growth rate $\dot{D}$ and initial volume V_i by combining Eq. (A.16) and Eq. (A.20), giving

$$\upsilon_r = f_1(s, \dot{D}, V_i). \tag{A.21}$$

Among these input parameters, V_i is a constant that can be calculated from the preform geometry. The ring thickness $s = s(t)$ is time dependent, obtainable from a sensor response of the mandrel position. Finally, putting in a desired constant ring growth rate ($\dot{D}$), a solution for υ_r can be obtained, as well as υ_a by using Eq. (A.20). The feed rates of the pressure rolls are now integrated in the adaptive motion control to give a constant ring growth rate.

Appendix B. Motion control

Wang (2010) developed an isothermal FE model of the hot ring rolling process with adaptive motion control of the guide and axial rolls, by utilizing Abaqus user subroutines. In this initial study, three motions, i.e., the rotational displacement of the guide arms around fixed hinges, the translational displacement of axial rolls in radial direction and rotation speed of the axial rolls are adaptively controlled by a sensor definition of the actual position of the measuring roll.

In the present paper, the control algorithm in Wang (2010) is further developed and adapted for controlling the feed rate program. Fig. B.1 shows how the opening angle of the guide roll arms α, is defined as a function of the machine geometry and the ring diameter change:

$$\alpha = \alpha_1 + \alpha_2 = \arctan\left(\frac{L_c + R}{L_a}\right) + \arccos\left(\frac{L_a^2 + (L_c + R)^2 + L_b^2 - \left(\frac{D_g}{2} + R\right)^2}{2L_b\sqrt{L_a^2 + (L_c + R)^2}}\right), \tag{B.1a}$$

with

$$R(t) = \frac{D(t)}{2} = \frac{R_0 + S_x(t)}{2}, \tag{B.1b}$$

where D_g is the guide roll diameter, R_0 is the initial ring radius, r is the current ring radius and S_x is the coordinate of the sensor node on the measuring roll. It is assumed that the ring always grows symmetrically to the rolling mill's axis and holds a good circularity. The origin of the global coordinate system is defined at the initial center of the ring workpiece. The measuring roll can only move along the rolling mill's axis with the ring.

Calculating the time derivative of α, gives

$$\dot{\alpha} = \frac{\mathrm{d}}{\mathrm{d}t}\alpha(S_x(t)) = f_{\dot{\alpha}}(S_x(t), \upsilon_x(t)), \tag{B.2}$$

where $\dot{\alpha}$ can be expressed as a function of S_x and the velocity of the sensor node υ_x. The rotational velocity of the guide roll arms around the fixed hinge, $\dot{\alpha}$, is then adaptively controlled using simulation response.

As noted in Appendix A, to ensure the prerequisite of the symmetry condition in Eq. (A.7), the rotation speed of the axial rolls n_A has to be adaptively controlled. This is realized here in conjunction with adaptive control of the translational displacement of the axial rolls in radial direction. Fig. B.2 shows schematically the adaptive motion control of the axial rolls from time point t_0 to time point t.

Aiming at minimizing the slip between the ring workpiece and the axial rolls, the virtual vertex of the conical axial roll coincides with the actual center of the ring workpiece during the entire process. In other words, when the mean velocity of the ring at the outlet of the axial roll gap υ_h is driven by the tangential velocity of the axial rolls υ_A (Eq. (A.4)), the same distribution of the tangential velocity in radial direction is expected for the ring workpiece and the axial rolls. The radial velocity of the axial rolls υ_{Ar} is thus equal to half of the ring growth rate and implemented in the subroutine as

$$\upsilon_{Ar}(t) = \frac{\upsilon_x(t)}{2}. \tag{B.3}$$

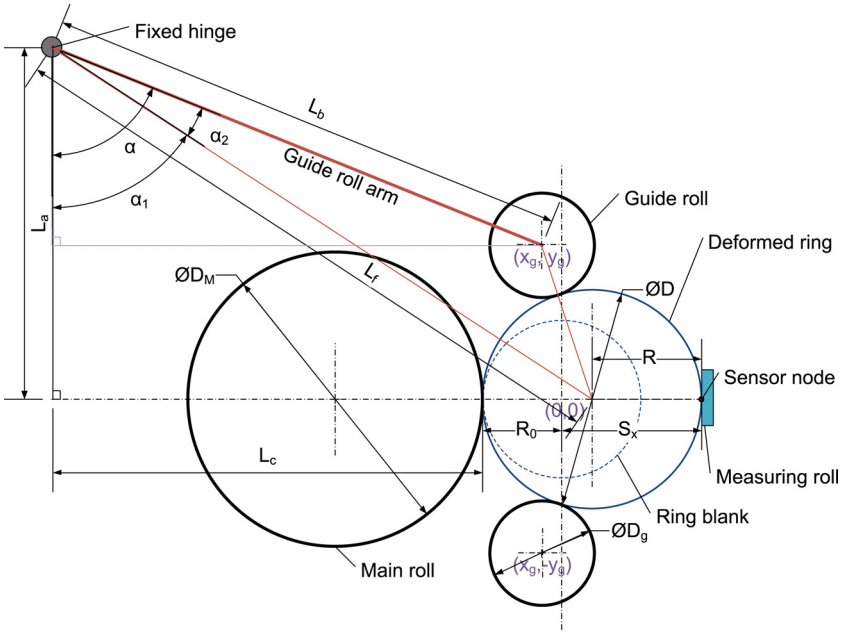

Fig. B.1. Motion control of guild rolls (Wang, 2010).

Simultaneously, the rotation speed of the axial rolls n_A is adaptively controlled for current time t as

$$n_A = \frac{30\upsilon_h}{\pi R_a}, \tag{B.4a}$$

with

$$R_a = R_m \sin(\alpha_3) = \frac{D_m}{2}\sin(\alpha_A), \tag{B.4b}$$

where R_a is the radius of the rotation plane of the axial rolls at the mean radius of the ring R_m, while α_A is the semi-vertical angle of

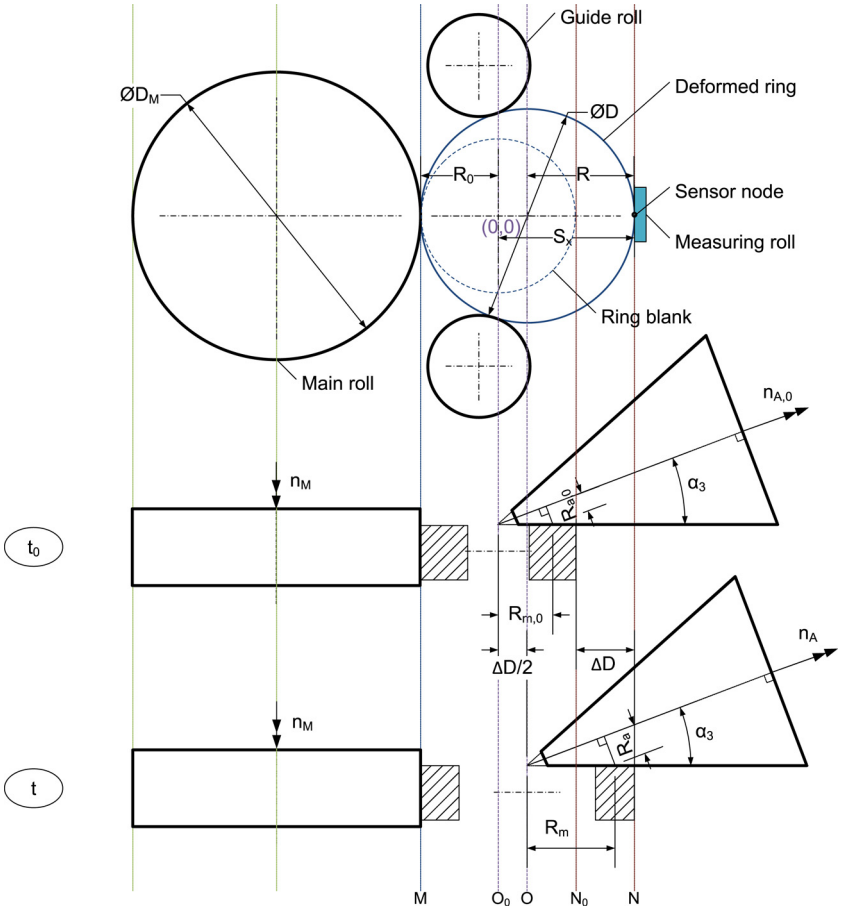

Fig. B.2. Motion control of axial rolls.

the conical axial rolls, as shown in Fig. B.2. Combining this with Eqs. (A.3), (A.7), (A.8), (A.12b), (A.12c), (A.14) and (A.15), including the machine information, gives

$$n_A = f_{n_A}(s, h, \upsilon_r, \upsilon_a, S_x). \tag{B.5}$$

In the above function, the inputs $s = s(t)$, $h = h(t)$, and $S_x = S_x(t)$ can be obtained from the actual positions of the mandrel, the upper axial roll and the measuring roll. The feed rates υ_r and υ_a are also calculated simultaneously using the mentioned sensor response. By knowing the explicit expression for the function f_{n_A} in Eq. (B.5), the rotation speed of the axial rolls is thereby adaptively controlled during the entire process.

References

Allwood, J.M., Tekkaya, A.E., Stanistreet, T.F., 2005. The development of ring rolling technology. Steel Res. Int. 76, 111–120, and 491–507.

Boucly, P., Oudin, J., Ravalard, Y., 1988. Simulation of ring rolling with new wax-based model materials on a flexible experimental machine. J. Mech. Working Technol. 16, 119–143.

Campbell, J., 2003. Castings, 2nd ed. Butterworth-Heinemann.

Dunne, F., Petrinic, N., 2005. Introduction to Computational Plasticity. Oxford University Press.

Hawkyard, J.B., Johnson, W., Kirkland, J., Appleton, E., 1973. Analyses for roll force and torque in ring rolling, with some supporting experiments. Int. J. Mech. Sci. 15, 873–893.

Kluge, A., Lee, Y.H., Wiegels, H., Kopp, R., 1994. Control of strain and temperature distribution in the ring rolling process. J. Mater. Process. Technol. 45, 137–141.

Koppers, U., Kopp, R., 1991. Geometrische und kinematische grundlagen beim ringwalzen. Steel Res. 62, 240–247.

Lin, H., Zhi, Z.Z., 1997. The extremum parameters in ring rolling. J. Mater. Process. Technol. 69, 273–276.

Mamalis, A.G., Hawkyard, J.B., Johnson, W., 1976. Spread and flow patterns in ring rolling. Int. J. Mech. Sci. 18, 11–16.

Olovsson, L., Simonsson, K., Unosson, M., 2005. Selective mass scaling for explicit finite element analyses. Int. J. Numer. Methods Eng. 63, 1436–1445.

Oyane, M., Sato, T., Okimoto, K., Shima, S., 1980. Criteria for ductile fracture and their applications. J. Mech. Working Technol. 4, 65–81.

Ryoo, J., Yang, D., Johnson, W., 1986. The influence of process parameters on torque and load in ring rolling. J. Mech. Working Technol. 12, 307–321.

Sun, Z., Yang, H., Ou, X., 2008. Thermo-mechanical coupled analysis of hot ring rolling process. Trans. Nonferr. Metals Soc. China 18, 1216–1222.

Sun, Z., Yang, H., Ou, X., 2010. Effects of process parameters on microstructural evolution during hot ring rolling of AISI 5140 steel. Comput. Mater. Sci. 49, 134–142.

Tiedemann, I., Hirt, G., Kopp, R., Michl, D., Khanjari, N., 2007. Material flow determination for radial flexible profile ring rolling. Prod. Eng. 1, 227–232.

Wang, C., 2010. Motion Control of the Rolling Tools in a Finite Element Model of the Ring Rolling Process. RWTH Aachen University (Master's thesis).

Wang, C., Geijselaers, H.J.M., Van Den Boogaard, A.H., 2013. Multi-stage FE simulation of hot ring rolling. AIP Conf. Proc. 1532, 1014–1019.

Yan, F.L., Hua, L., Wu, Y.Q., 2007. Planning feed speed in cold ring rolling. Int. J. Mach. Tools Manuf. 47, 1695–1701.

Zhou, J., Wang, F.L., Wang, M.H., Xu, W.J., 2011. Study on forming defects in the rolling process of large aluminum alloy ring via adaptive controlled simulation. Int. J. Adv. Manuf. Technol. 55, 95–106.